

Volcano-wide fringes in ERS synthetic aperture radar interferograms of Etna (1992-1998): Deformation or tropospheric effect ?

François Beauducel and Pierre Briole

Département de Sismologie, UMR CNRS 7580, Institut de Physique du Globe, Paris

Jean-Luc Froger

Laboratoire Magmas et Volcans, UMR CNRS 6524, Université Blaise Pascal, Clermont-Ferrand

Abstract. Mount Etna (3300 m) is the volcano that has been first and most studied by differential synthetic aperture radar. Previous papers gave evidence for a large-scale deformation of the entire edifice consistent with unrest episodes but with a poor fit with classical elastic models. Also, atmospheric effects on mountainous areas are known to be very significant. Accordingly, interferograms may reflect both deformation and tropospheric effects. We investigate here the possibility of evaluating and correcting tropospheric effects directly from the interferograms. From 38 ERS synthetic aperture radar ascending scenes taken from 1992 to 1999, we have computed 238 interferograms. The amount of data allows us to analyze how the coherence is maintained over long periods of time and thus how it reveals the location of permanent scatters. From a simple analysis of phase-elevation relation, we give evidence for the clear difference in pattern between stratified tropospheric effects and large-scale deformation produced by a source in a Three-dimensional elastic body with topography. Using combination of inversion processes, we analyze both deformation source and tropospheric effects for the complete set of 238 interferograms. Finally time evolution of the parameters and modeling probability estimation are retrieved for each SAR image. Estimated relative change in tropospheric delay varies in time from -2.7 to $+3.0$ (± 1.2) fringes. They are consistent with other tropospheric estimations at Etna based on ground met and Global Positioning System observations on the same period of time. Magmatic volume variations remain below error bars and thus cannot be estimated properly. Finally, some of the interferograms may be entirely explained by the difference in tropospheric conditions between the two acquisition periods, without the need to invoking a deformation of the volcano.

1. Introduction

Differential synthetic aperture radar interferometry (DInSAR) constitutes a unique tool for the remote sensing of displacement fields at large scale and high spatial resolution [Massonnet and Feigl, 1998]. Mount Etna is the first and most studied volcano for which DInSAR has been used. Massonnet *et al.* [1995] revealed a large-scale deflation of the volcano on the 1992-1993 period, interpreted as an elastic response of the body to a volume decrease in a 16-km-deep magma chamber. Lanari *et al.* [1998] showed that this deflation was followed by an inflation during the period 1993 to 1995. At the local scale, Briole *et al.* [1997] showed a clear correlation between DInSAR fringes in the Valle Del Bove and the location of the 1986-1987 and 1989 lava fields. This deformation was interpreted as a combination of a lava field compaction still significant several years after eruption and a viscoelastic relaxation of the surrounding material. Local-scale deformation fields determined by DInSAR are very reliable and cannot be biased by propagation artifacts in the troposphere and ionosphere unless these effects are very local. For large-scale deformation fields, Delacourt *et al.* [1998] proposed that tropospheric delay may produce volcano-wide effects up to ± 1.5

fringes thus limiting to ± 5 cm the detectability of the method in long-wavelength domain. Accordingly, the problem of eliminating tropospheric artifacts is a most serious one at the moment if the accuracy of the DInSAR methods to be improved.

In this paper, we investigate the possibility of retrieving tropospheric information from the DInSAR image itself by analyzing the correlation between pixels altitude and phase value. This work implies several successive steps that provides us with additional outputs and understanding not directly linked with the troposphere. Indeed, the analysis of altitude-phase regression requires the need of selecting a subset of pixels that maintain their coherence over the duration of the interferograms. Using a combination of inversion processes, we analyze both deformation source and tropospheric effects for a large set of interferograms on Mount Etna, and finally retrieve time evolution of the parameters and estimate the model probability.

2. Data Acquisition

From 38 ERS-1 and ERS-2 ascending orbits images on the 1992 to 1999 period (see Table 1), 238 interferograms were computed using the Diapason software [Centre National d'Études Spatiales, 1996]. The digital elevation model (DEM) of Etna area was obtained by merging four different types of data then validated using >100 km of kinematic Global Positioning System (GPS) profiles [Briole *et al.*, 1999]. Its altimetric root-mean-square (RMS) is estimated to be 3.5 m. Thus, theoretically, it allows interferogram processing with 99% of the combinations of two images with an altitude of ambiguity (AA) >10 m, to have

Copyright 2000 by the American Geophysical Union.

Paper number 2000JB900095.
0148-0227/00/2000JB900095\$09.00

less than one residual fringe of topography. The 238 computed interferograms have an AA >30 m limiting DEM errors effects to a third of fringe with 99% of confidence. The intersection of SAR image and DEM locations allow to investigate the whole area, i.e., 55×55 km (Figure 1).

Figure 2 shows the relative orbit baselines versus image date, and each computed interferogram is represented by a line between two images. This mode of representation mimics a geodetic network and illustrates how a global data adjustment can be used to retrieve parameters relative to single images from data relative to the interferograms. Following this comparison with a geodetic network, Figure 2 shows that our DInSAR data network is homogeneous and well constrained with a redundancy factor equal to 6.4.

A list of the 238 interferograms with several relevant parameters is reported in Table 2. Time periods for the computed interferograms vary from 1 day to more than 6 years. In particular, we have seven 1-day (Tandem mission) and seven 35-day interferograms.

3. DInSAR Processing Tools

3.1. Phase Coherence and Interferogram Classification

Investigation for coherent pixels has been done in different successive steps. For each interferogram we classified the coherence of the pixels using three different approaches ((1) output of Diapason software, (2) amplitude-based coherence, (3) phase-gradient) that gave relatively comparable results. The phase gradient method, which we used in this paper, consists of computing within a 3×3 pixel square the difference of phase values between each pixel and the eight contiguous ones. For each pixel the phase difference with the eight neighbors is compared to a threshold value, and the coherency is given by the number of neighbors that differ from the central pixel value by less than the threshold. In this paper, we fixed the gradient threshold to 16% of 2π phase over 25-m pixel (0.04 rad/m).

We started our analysis by a visual assessment of the whole database. An objective grade Q was assigned to each interferogram, as an average of coherence value over all pixels, reduced to an integer between 0 and 4. This translates a global quality factor of the interferogram: $Q = 0$, poor coherent areas; $Q = 4$, excellent coherence. We obtained six interferograms with $Q = 0$, 182 with $Q = 1$, 40 with $Q = 2$, 3 with $Q = 3$, and seven with $Q = 4$. In the following sections of this paper, this classification has been used for interferogram selection and data weighting.

3.2. Constitution of the Collective Mask

For the 238 available interferograms the above individual coherency images have been stacked and scaled into the 0-255 range in order to obtain a global “collective” coherency map (CM) (Figure 3). The CM reflects the location of the areas of at least a few pixels where the coherency is maintained over relatively long periods of time (the average duration of the interferograms is 823 days, i.e., 2.25 years). The areas that keep more coherency are, on one hand, the recent lava flows and some more ancient pahoeha lava fields not yet covered by the vegetation and, on the other hand, the towns. This property has been already mentioned by other studies [Le Toan *et al.*, 1998; Ferretti *et al.*, 1999]. The originality of our CM is that it is based on a large number of images and consequently is expected to have a higher spatial resolution. It is also expected to be less affected by local and temporal effects related to volcano deformations or local tropospheric effects.

The CM has been used to filter the interferograms in order to retain only the less noisy pixels. Figure 4a shows an example of interferogram from original data, and Figure 4b shows the corresponding masked image obtained with keeping the phase values that correspond to $CM \geq 50\%$.

3.3. Two-Dimensional Interpolation and Automatic Fringes Counting

Applying the CM on each interferogram, the selected set of most coherent pixels constitutes an incomplete image. We interpolate between coherent pixels using the “nearest-neighbor” method based on two-dimensional (2-D) Delaunay triangulation [Fortune, 1987]. This method fills the “blanks” by creating areas of constant values equal to the nearest neighbor data. It is the fastest way to interpolate and, contrary to some other interpolation methods, it does not affect the data and allows to keep the phase jumps intact (Figure 5), a condition necessary for further phase unwrapping.

For fringes counting, we selected 100 contiguous linear profiles from Catania (about 0-m elevation) to the summit of Etna (3300 m). These profiles constitute a 100×1200 pixel area that contain very coherent lava flows and is almost radial to the volcano (Figure 1). Applying the CM and the 2-D interpolation described above (Figure 6), phase profiles are unwrapped independently as 1-D signals, and the summit unwrapped phase value is determined as the average of the 100 profiles (see example in Figure 7). Application of this method to 100 parallel profiles provides means to determine a standard deviation on the counted number of fringes. The number of automatic counted fringes ΔF_{obs} and standard deviation S_{DF} for all interferograms are reported in Table 2. For ERS-1 and ERS-2 a fringe corresponds to a half wavelength delay, i.e., 2.8 cm.

3.4. Retrieval of a Relative Fringe Parameter for Each Single ERS Scene

As can be seen in Figure 2, there are closures between the different interferograms. It is thus possible to compensate the automatic counted fringes numbers (section 3.3), in the same way as one would compensate a geodetic network. This is a typical overdetermined least squares problem with m data with covariance \mathbf{V} and n unknown, with $m > n$. We solved the linear system $\mathbf{A}\mathbf{X} = \mathbf{B} + \mathbf{E}$, where \mathbf{A} is the design matrix (contains only values of -1 , 1 , or 0), \mathbf{B} is the vector of data (238 values determined by fringe counting per interferogram DF_{obs}), \mathbf{E} is normally distributed with zero mean and covariance \mathbf{V} , and \mathbf{X} is the vector of 38 parameters corresponding to an individual relative fringe parameter per image. This classical linear algebra solution to this problem is given by [Graybill, 1976]

$$\mathbf{X} = (\mathbf{A}^T \mathbf{V}^{-1} \mathbf{A})^{-1} \mathbf{A}^T \mathbf{V}^{-1} \mathbf{B} , \quad (1)$$

and a posteriori uncertainties may be estimated by

$$\Delta \mathbf{X} = \sqrt{\frac{(\mathbf{A}^T \mathbf{V}^{-1} \mathbf{A})^{-1} \mathbf{B}^T (\mathbf{V}^{-1} - \mathbf{V}^{-1} \mathbf{A} (\mathbf{A}^T \mathbf{V}^{-1} \mathbf{A})^{-1} \mathbf{A}^T \mathbf{V}^{-1}) \mathbf{B}}{m - n}} . \quad (2)$$

This data inversion translates information relative to interferograms (i.e., pairs of scenes) into information relative to single ERS scenes. When looking to temporal changes on the volcano, results relative to single scenes are much easier to interpret than differential data involving a pair of images.

Table 1 and Figure 8 present the results of the adjustment and give the maximum relative delay expressed in fringes for each image and standard deviation. Estimated errors range from 0.3 to

0.5 fringe. Table 2 gives the calculated maximum differential delay DF_{cal} for each interferogram, which can be compared to observed values DF_{obs} . The RMS of the 238 residues equals 1.1 fringe, a value that reflects the average error on fringe counting, mostly due to the 38 low coherent interferograms ($Q=0$) that were also introduced in the inversion. The other partial RMS are (in fringe): 0.8 for $Q \geq 1$, 0.5 for $Q \geq 2$ and 0.2 for $Q \geq 3$. The residuals on the data for $Q \geq 2$ are then of the same order as the estimated a posteriori errors on the parameters, i.e., ~ 0.5 fringe.

The curve in Figure 8 is expected to contain both a tropospheric contribution and the state of deformation at the time of the image. Assuming that the deformation of the volcano does not exhibit temporal high frequencies at large scale, a property that is confirmed, for example, by the absence of sudden tilt at large scale during the considered period (G. Puglisi, kick-off meeting of Emedocle project, Rome, Sept. 1998), we propose that fast movements at large scale in the signal are more likely explained by tropospheric effect. The presence of periodic (annual) negative peaks on September-November each year (except for 1994, for which no data are available) suggests some meteorological effects due to seasonal variations of atmospheric parameters. This simple analysis of frequencies does not allow the proper separation of the respective contribution of troposphere and deformation. Additional considerations are mandatory if one wishes to do so.

4. Tropospheric and Deformations Modeling

4.1. Phase-Elevation Relation in Stratified Troposphere

In this paper, we suppose that the troposphere is horizontally homogeneous in the considered 55×55 km area. This is a first-order approach of atmospheric effects, since Tandem interferograms, for example, show horizontal variations of phase in flat areas, which cannot be attributed to ground deformation. However, local effects on Tandem interferograms remain smaller than a fraction of fringe. Our hypothesis of simply layered troposphere leads to a phase delay on the interferogram that depends only on the altitude of the corresponding pixel (Figure 9) and thus a relation between phase and elevation that is independent on the horizontal position of the pixel. In the following, we assume that the troposphere can be modeled by horizontal layers from sea level to the top of the volcano.

It is important to observe that the deformation field predicted theoretically by simple point source model [Mogi, 1958] (Figure 9) shows no correlation between phases and elevation over Etna. This is due both to the facts that the volcano is not axisymmetric and the modeled fringes are shifted and deformed by several kilometers with respect to the axis of the volcano, because of the oblique SAR line of sight. When using a more complex model taking into account topography [Cayol and Cornet, 1998], the absence of correlation is even worse.

This simple analysis indicates that when a strong correlation between topography and phase exists, it is more likely to be interpreted, at the first order, as due to a tropospheric contribution than to a deformation. Indeed, according to our simple models, large deformation produced by a hypothetical simple source should produce a phase noise that would hide any phase-elevation relation. To the contrary, the observation of a clear phase-elevation relation (without noise) excludes any large deformation effect. If both effects are present, i.e., troposphere and deformation, with the same order of magnitude, no correlation is expected to be observed and it might be impossible to separate the two signals using this approach, without any other information on the deformation field. However, since the two

effects are very different in pattern on the resulting phase (compare Figure 4c and 4d), we may conduct a global inversion in order to retrieve at the same time tropospheric and deformation parameters.

4.2. Constitution of the Equally Spaced Altitude Mask

The CM cannot be used directly for a phase-elevation analysis because the best pixels are not equally distributed in elevation and are often concentrated in some highly coherent lava flows. We computed, for every 50-m elevation layer, two selections of the best 20 pixels (belonging to the CM), one for the Etna area and one for the surrounding area (see the limit of these two areas in Figure 1). This allows us to establish a new map of the 1686 most coherent pixels of Etna, either spatially (horizontal and vertical) or temporally, which we named equally spaced altitude mask (ESAM, Figure 10). Since the pixels of the ESAM are relatively well spaced horizontally, they are able to correctly detect any deformation effects at large scale that would be mainly dependent on the radial distance from the summit. Note that ESAM do not keep coherent pixel in the last 3000-3300 m interval.

This research of the coherent pixels was complicated by the fact that residual errors in the satellite orbits generate long-wavelength parallel fringes (tilts) that creates noise into the altitude-phase relation. An additional problem is the fact that there is a trade-off between the value of these parasitic tilts and the identification of coherent pixels in the altitude-phase regression. In practice, we used different approaches to calculate these tilts: first, using the pixels issued from the CM, and second, using the pixels located at an elevation of 500-550 m at the base of the volcano edifice. The estimated tilt appeared not to be reliable in all cases, but it was reliable in general for the interferograms with AA larger than 150-200 m that are also more coherent in average.

4.3. Joint Inversion of Tropospheric Delay and Deformation Source per Interferogram

Using the ESAM, we constituted a database of phase values, global coherencies, and pixel positions for the 238 interferograms. It was not possible to invert a deformation source (assuming the point source formalism) and tropospheric effects per image because it would have constituted a 190-parameter model (depth and volume variation for the source and four parameters for tropospheric profile times 38 images), in particular, because the forward problem is highly nonlinear. Instead, we assumed a deformation source located at a fixed position, 6 km below the summit, i.e., a depth consistent with those proposed by Bonaccorso [1996] and Lanari *et al.* [1998]. This allowed inversion of the data for each interferogram and then adjustment of the results for single images (as made previously for the maximum delay study), since the deformation model has become linear. Again, another interesting consequence of processing interferograms independently is to allow an error estimation of the model through the compensation.

The forward problem is defined as follows: displacement vectors are computed for each pixel position with Mogi's [1958] model, considering a volume variation ΔV in a 6-km-deep source below the summit. The displacements are then converted into phase value by the projection on the satellite line of sight for ascending orbit and wrapping around the half wavelength. The differential tropospheric delay is computed for each pixel elevation from a smooth vertical profile described with a fourth-degree polynomial that fits five points: values for 0 m, 1000 m, 2000 m, and 3000 m are parameters and a last point at 3500 m is

fixed equal to the 3000 m value in order to avoid polynomial border effects. The model is then defined as a vector \mathbf{m} of five parameters (one for deformation source and four for tropospheric profile). For a given model \mathbf{m} , we compare observed and calculated values of phase using the *Vadon and Sigmundsson* [1997] method: for each pixel i , differences between observed phase $\mathbf{j}_{\text{obs}}^i$ and computed phase $\mathbf{j}_{\text{cal}}^i(\mathbf{m})$ are summed as complex numbers, so the final modulus is maximum when phases differences are constant in average. We extended this method by using the CM value w_i as a weight for each pixel, i.e., the complex number magnitude. The likelihood (or fitness) function to be maximized is then defined as

$$L(\mathbf{m}) = \left| \sum_i w_i e^{j2p(\mathbf{j}_{\text{obs}}^i - \mathbf{j}_{\text{cal}}^i(\mathbf{m}))} \right|. \quad (3)$$

The inverse problem is described by six parameters and 1686 data, for each interferogram. The fitness function is highly nonlinear and contains many local maxima (mainly because of the phase ambiguity). Accordingly, inversion was performed in two steps.

First, we used a genetic algorithm (GA: for a review and definition of terms, see *Gallagher et al.* [1991]) to find the approximate maximum of fitness function. After various attempts, we fixed the population size to 500, crossover probability to 1, mutation probability to 0, and parameter encoding to 6 bits. The large number of individuals per population tends to be close to a Monte Carlo algorithm that explores the whole model space, in order to avoid possibly missing the best solution. The algorithm converges in most of the cases in 10 generations or less.

Second, starting from the GA result, we used the gradient-search method to minimize the misfit function locally. This step is very fast and allows us to refine the solution.

This has been done for the 238 interferograms. Complete inversion processing takes about 10 hours on a Sparc Ultra 10 station. Figure 11 shows two examples of data and modeling results: for interferogram 54 (September 1992 to October 1993) and interferogram 108 (May 1993 to September 1995). For both, the volume variation is found to have insignificant value, and almost all the signal can be reproduced by the tropospheric effect. The inversion did not converge in all the cases, and some of the interferograms did not allow a correct fitting. For most of these misfitted interferograms, the difficulty is likely due to the noise on the data, but it is also obvious that both simple tropospheric and deformation models cannot fit all of the observations.

4.4. Compensation of the Results: Troposphere and Deformation per Image

The results from the differential modeling on each interferogram are then compensated to retrieve an estimate of individual parameter for each single ERS image. In addition to the importance for data interpretation this analysis constitutes an important step for model validation, since the modeling for individual interferogram contains a significant number of misfitted data, as mentioned above. Each previous interferogram result has been weighted by the quality factor Q here as defined above.

The inverse problem is constituted by 6×38 parameters and 6×238 data, and the forward problem is strictly linear and can be solved by a matrix inversion (see equations (1) and (2)). Table 1 presents the final modeling results per image: the volume of the source V and the four values of tropospheric delay per altitude layer. All the reported values for tropospheric delay are relative

and may be shifted by a constant. Here their average was assumed to be zero. This means that the population of interferograms is supposed to constitute a representative sample of the diversity of tropospheric conditions on Etna. A posteriori uncertainties are given for the source volume and 3000-m tropospheric delay. The inferred temporal evolution of source volume of the volcano and tropospheric profiles for the 1992-1998 period are plotted in Figure 12.

A posteriori errors at 3000-m elevation for the tropospheric parameters are of the order of 1.2 fringe in average. The computed profiles present large variations, inversions, and high-frequency modulations well above the 1.2 fringes error bar. This demonstrates that to first order, most of the fringes observed in interferograms of Mount Etna may be due to troposphere rather than to deformation. For instance, the estimated tropospheric delays between the two orbits 20658 and 00985 (August 27 and 28, 1995) imply a differential large-scale tropospheric effect of -2.8 ± 1.5 fringes in 1 day. This confirms *Massonnet and Feigl's* [1998] conclusion that the observed signal in Tandem interferogram 193 corresponds to a large atmospheric effect. Our analysis diminishes significantly the estimation of the amount of large-scale deformation that occurred on Mount Etna since 1992, as compared to results estimated in previous studies.

The 1.2 fringe typical error on troposphere delay determination corresponds to about $5 \times 10^6 \text{ m}^3$ in equivalent deformation. According to those error bars (one standard deviation) our analysis of the magma source evolution at Etna is as follows: a rapid deflation in 1992, followed by a stable period over 1993 to 1996 (note there are no data for 1994) with two short periods of inflation at the ends of 1993 and 1995, then a slow inflation in 1997 until the last available data in 1998. However, all the above changes are now between -6 and $+14 \times 10^6 \text{ m}^3$, this is much less than the estimates of the previous studies.

Part of the tropospheric variations seem to be annual. For some images for the 1993 to 1994 period the value of tropospheric correction at the summit (at 3000-m elevation) has been compared to values predicted by *Delacourt et al.* [1998] from a model based on ground met data and calibrated by radiosonde measurements. There is a good qualitative correlation between the two results: high delay in November 1992 and October 1993 and lower delay in June 1993, but our study predicts a much larger effect, lasting from -1.4 to $+2.4$ fringes instead of ± 0.6 fringes for the considered period. We also compared our results with tropospheric delay computed from GPS measurements at Etna, for the October 1996 to October 1997 period (A. Bonforte et al., Calibration of atmospheric effects on SAR interferograms by GPS and local atmosphere models: Firsts results, submitted paper to *Journal of Atmospheric and Terrestrial Physics*, 1999). There is a good agreement between the two estimates of delays (Figure 13), considering estimations of RMS scatters equal to 3.6 cm for InSAR and 2.5 cm for GPS. Because the two types of results are independent, this strongly enhances our confidence in our results.

An example of modeled interferogram is given in Figure 4c. In comparison, the model of deformation source proposed by *Cayol and Cornet* [1998] is shown in Figure 4d. The best fit of the observations to our model is obvious. It can also be seen that the few fringes located in the surrounding area (especially the northern mountains) are well reproduced by the model. This is not the case with the deformation model. Figure 14 presents the residues after the removal of modeled tropospheric and deformation effects.

5. Conclusion

The use of a large number of interferograms allowed us to compensate the various differential results to retrieve tropospheric and deformation parameters relative to single SAR images into a time-based representation. Even for basic investigations like the analysis of maximum delay (fringe counting), we think that our global and systematic approach helps to clarify and validate the observations, avoiding possible misinterpretation of individual DInSAR. This study also brings some validated tools for DInSAR analysis. Collective mask of coherence, reliable phase filtering and interpolation, and automatic fringe counting could be applied at other areas of interest when several interferograms are available.

Unless orbital effects are correctly removed in the interferogram calculation, tropospheric effects can hardly be estimated from the interferograms themselves without an a priori model for the source of deformations. We show in this paper that theoretical phase delays produced on Etna by simple elastic modeling are very different from phase delays produced by a stratified tropospheric model with regard to the phase-elevation relation. Simple deformation patterns have been frequently observed on many volcanoes with classical geodetic methods like leveling (Sakurajima, Krafla, Campi Flegrei, etc.). In these instances, elastic modeling was found to describe precisely and in a satisfactory way the displacement field, even with simple source shape [Dvorak and Dzurizin, 1997]. This good agreement is mainly due to the poor dependency of surface vertical displacements on the deformation source shape. Concerning DInSAR observations, which contain 90% of the vertical component of displacement, evidence for simple elastic deformation fields has been widely proved on fault areas (co-seismic at Landers [Massonnet et al., 1993]) and even, more recently, on volcanic areas (deflation at Campi Flegrei [Avallone et al., 1999] and eruptive fissure at Piton de la Fournaise [Sigmundsson et al., 1999]). On Mount Etna, SAR data for the period 1992-1999 do not show such a pattern simply related to an elastic deformation model, and the first-order signal can be more easily interpreted as a tropospheric contribution. Our study shows that it is possible to estimate the tropospheric contribution with an average error of 1.2 fringes (range from 0.6 to 1.7) for individual ERS scenes, when this parameter is estimated jointly with a deformation parameter. When only the number of fringes is inverted, without a priori model of deformation or troposphere, the a posteriori error range is lower, of the order of 0.5 fringes. Although the joint inversion is expected to be more rigorous, it turns out that it creates much larger uncertainties in the estimated results. For this reason, the use of data in the surrounding regions of the volcano to estimate the tropospheric delay would constitute an important step forward in the method. This step would be possible if more accurate orbits were available, not implying the removal of regional orbital fringes in the data before fringe analysis. Another possible step would be to understand whether the pixels that were removed from ESAM because of their systematic shift from a smooth phase-elevation relation could be recovered by applying a possible offset mask on the CM. As the CM and ESAM are expected to be information characteristic of the volcano and reliable for the medium to long term, such effort might be worth doing. Finally, the large-scale deformation of the volcano appears to be significantly less than estimated in previous studies. Volume fluctuations within the assumed reservoir at 6-km depth remain in the range -8 to $+14 \times 10^6$ m³, with average error bars of 5×10^6 m³. Corresponding vertical changes at volcano summit range between -5 and $+9$ cm, and the corresponding maximum tilts predicted by our study range

between -8 and $+13$ μ rad.

Acknowledgments. Numerical processing on interferograms has been developed and performed using the Matlab 5 software. Thanks to V. Cayol, C. Delacourt, D. Remy, and F.H. Cornet for useful discussions and to all other "Madviews" project participants for comments during the final meeting in Paris. This paper has been very significantly improved thanks to comments by T.A. Herring and two anonymous reviewers. This work has been supported by EU contract ENV4-CT96-0294 and French PNRN project "Radar Interferometry on Volcanoes". There is also an IPGP contribution #1671.

References

- Avallone, A., P. Briole, C. Delacourt, A. Zollo, and F. Beauducel, Subsidence at Campi Flegrei (Italy) detected by SAR interferometry, *Geophys. Res. Lett.*, 26, 2303-2306, 1999.
- Bonaccorso, A., Dynamic inversion of ground deformation data for modelling volcanic source, *Geophys. Res. Lett.*, 23, 451-454, 1996.
- Briole, P., D. Massonnet, and C. Delacourt, Post-eruptive deformation associated with the 1986-87 and 1989 lava flows of Etna detected by radar interferometry, *Geophys. Res. Lett.*, 24, 37-40, 1997.
- Briole, P., A. Avallone, F. Beauducel, A. Bonforte, V. Cayol, C. Deplus, C. Delacourt, J.-L. Froger, B. Malengreau, and G. Puglisi, Interférométrie radar appliquée aux volcans: cas de l'Etna et des Champs Phlégréens (Italie), in *Rapport Quadriennal CNFGG 1995-1998*, pp. 121-128, J.-P. Barriot Ed., Obs. Midi-Pyrénées, Toulouse, France, 1999.
- Cayol, V., and F.H. Cornet, Effects of topography on the interpretation of the deformation field of prominent volcanoes: Application to Etna, *Geophys. Res. Lett.*, 25, 1979-1982, 1998.
- Centre National d'Études Spatiales (CNES), Philosophie et mode d'emploi de la chaîne logicielle interférométrique DIAPASON, Toulouse, France, 1996.
- Delacourt, C., P. Briole and J. Achache, Tropospheric corrections of SAR interferograms with strong topography: Application to Etna, *Geophys. Res. Lett.*, 25, 2849-2852, 1998.
- Dvorak, J.J., and D. Dzurisin, Volcano geodesy: The search for magma reservoirs and the formation of eruptive vents, *Rev. Geophys.*, 35, 343-384, 1997.
- Ferretti, A., C. Prati, and F. Rocca, Multibaseline InSAR DEM reconstruction: The Wavelet approach, *IEEE Trans. Geosci. Remote Sens.*, 37, 705-715, 1999.
- Fortune, S.J., A sweepline algorithm for Voronoi diagrams, *Algorithmica*, 2, 153-174, 1987.
- Gallagher, K., M. Sambridge, and G. Drijkoningen, Genetic Algorithms : An evolution from Monte Carlo methods for strongly non-linear geophysical optimization problems, *Geophys. Res. Lett.*, 18, 2177-2180, 1991.
- Graybill, F., *Theory and Application of the Linear Model*, 207 pp., Duxbury, Boston, Mass., 1976.
- Lanari, R., P. Lundgren, and E. Sansosti, Dynamic Deformation of Etna Volcano observed by satellite radar interferometry, *Geophys. Res. Lett.*, 25, 1541-1544, 1998.
- Le Toan, T., J. Askne, A. Beaudouin, M. Hallikainen, S. Quegan, L. Ulander, and U. Wegmuller, Eufora: European forest observations by radars, paper presented at Progress in Electromagnetics Research Symposium (PIERS), Session J1, July 13-17, Nantes, France, 1998.
- Massonnet, D., and K. L. Feigl, Radar interferometry and its application to changes in the Earth's surface, *Rev. Geophys.*, 36, 441-500, 1998.
- Massonnet, D., M. Rossi, C. Carmona, F. Adragna, G. Peltzer, K. Feigl, T. Rabaut, The displacement field of the Landers earthquake mapped by radar interferometry, *Nature*, 364, 138-142, 1993.
- Massonnet, D., P. Briole, and A. Arnaud, Deflation of Mount Etna monitored by spaceborne radar interferometry, *Nature*, 375, 567-570, 1995.
- Mogi, K., Relations between the eruptions of various volcanoes and the deformations of the ground surfaces around them, *Bull. Earthquake Res. Inst. Univ. Tokyo*, 36, 99-134, 1958.
- Sigmundsson, F., P. Durand, and D. Massonnet, Opening of an eruptive fissure and seaward displacement at Piton de la Fournaise volcano measured by RADARSAT satellite radar interferometry, *Geophys. Res. Lett.*, 26, 533-536, 1999.
- Vadon, H., and F. Sigmundsson, Crustal deformation from 1992 to 1995 at the Mid-Atlantic Ridge, southwest Iceland, mapped by satellite radar interferometry, *Science*, 275, 193-197, 1997.

F. Beauducel and P. Briole, UMR CNRS 7580 Sismologie, Institut de Physique du Globe de Paris, Case 89, 4 place Jussieu, 75252 Paris Cedex 05, France. (beauducel@ipgp.jussieu.fr; briole@ipgp.jussieu.fr).
J.-L. Froger, UMR CNRS 6524 Magmas et Volcans, Université Blaise Pascal, Clermont-Ferrand, France.

(Received April 21, 1999; revised February 1, 2000; accepted March 16, 2000.)

Table 1. SAR ERS-1 and ERS-2 Images

Date	ERS	Orbit	N_{inter}	$F_{\text{cal}} \pm s$ (Fringe)	$V \pm s$ (10^6 m^3)	Tropospheric Delay per Altitude (Fringe)			
						0 m	1000 m	2000 m	3000 m ($\pm s$)
Aug. 23, 1992	1	05785	14	-0.0 \pm xx	0.0 \pm xx	0.0	0.0	0.0	0.0 \pm xx
Sept. 27, 1992	1	06286	15	-1.0 \pm 0.3	2.3 \pm 3.8	-0.6	-2.1	-2.6	-2.3 \pm 1.1
Nov. 01, 1992	1	06787	13	-1.0 \pm 0.3	-0.1 \pm 3.9	-0.2	-1.7	-2.0	-1.8 \pm 1.2
May 30, 1993	1	09793	15	2.9 \pm 0.3	-1.9 \pm 3.4	0.0	0.1	1.3	1.4 \pm 1.0
July 04, 1993	1	10294	16	1.9 \pm 0.3	-1.1 \pm 3.7	-0.0	-0.5	0.5	1.0 \pm 1.1
Aug. 08, 1993	1	10795	10	1.2 \pm 0.3	4.0 \pm 3.8	0.0	-0.9	0.5	0.7 \pm 1.1
Sept. 12, 1993	1	11296	10	-0.9 \pm 0.3	4.8 \pm 3.8	-0.1	-1.5	-1.6	-0.8 \pm 1.1
Oct. 17, 1993	1	11797	16	1.9 \pm 0.3	-0.9 \pm 3.8	0.1	-1.0	0.1	0.0 \pm 1.1
Nov. 21, 1993	1	12298	13	0.8 \pm 0.4	6.5 \pm 4.6	0.2	0.3	0.6	0.5 \pm 1.4
June 27, 1995	1	20658	11	0.9 \pm 0.4	-7.2 \pm 4.9	0.1	0.3	-0.2	0.3 \pm 1.5
June 28, 1995	2	00985	9	-1.2 \pm 0.4	-2.7 \pm 5.3	0.1	-1.0	-2.0	-2.5 \pm 1.6
Aug. 01, 1995	1	21159	15	-2.5 \pm 0.3	3.6 \pm 3.5	-0.5	-1.8	-2.7	-2.1 \pm 1.0
Aug. 02, 1995	2	01486	17	-0.8 \pm 0.3	-1.0 \pm 3.5	-0.2	-1.1	-1.5	-1.6 \pm 1.1
Sept. 05, 1995	1	21660	11	-1.1 \pm 0.4	-1.7 \pm 5.0	0.0	-1.3	-2.2	-1.8 \pm 1.5
Sept. 06, 1995	2	01987	9	-0.4 \pm 0.4	-4.7 \pm 5.3	0.3	0.2	-0.2	-1.5 \pm 1.6
Oct. 10, 1995	1	22161	12	-1.0 \pm 0.3	1.9 \pm 3.6	-0.5	-0.8	-1.2	-1.3 \pm 1.1
Oct. 11, 1995	2	02488	4	-1.0 \pm 0.6	4.1 \pm 5.5	0.4	-0.8	-0.9	0.7 \pm 1.6
Nov. 14, 1995	1	22662	11	-0.7 \pm 0.4	-4.1 \pm 5.0	-0.1	0.5	-0.6	-1.0 \pm 1.5
Nov. 15, 1995	2	02989	6	-0.7 \pm 0.5	-3.3 \pm 5.8	-0.4	-0.8	-1.7	-2.7 \pm 1.7
Dec. 19, 1995	1	23163	9	-0.8 \pm 0.3	5.3 \pm 3.9	-0.2	-1.3	-1.0	1.1 \pm 1.2
Dec. 20, 1995	2	03490	16	-0.1 \pm 0.3	5.1 \pm 3.3	-0.2	-0.6	-0.7	0.2 \pm 1.0
Aug. 21, 1996	2	06997	13	-1.4 \pm 0.4	-4.1 \pm 4.6	-0.2	-0.4	-2.2	-1.7 \pm 1.4
Sept. 25, 1996	2	07498	15	-0.9 \pm 0.3	0.7 \pm 3.7	0.0	0.7	-0.4	0.6 \pm 1.1
Oct. 30, 1996	2	07999	11	-0.2 \pm 0.3	4.3 \pm 3.7	-0.0	0.5	0.6	1.5 \pm 1.1
Jan. 08, 1997	2	09001	15	0.6 \pm 0.4	-3.4 \pm 3.9	0.0	0.8	0.1	1.1 \pm 1.2
March 19, 1997	2	10003	15	1.2 \pm 0.4	-0.9 \pm 4.2	-0.1	0.3	-0.1	0.7 \pm 1.3
May 28, 1997	2	11005	15	0.9 \pm 0.3	1.7 \pm 4.1	0.2	1.7	0.9	1.8 \pm 1.2
Sept. 10, 1997	2	12508	13	-1.5 \pm 0.4	0.9 \pm 4.6	0.0	0.9	-0.5	-0.2 \pm 1.4
Oct. 15, 1997	2	13009	15	-0.0 \pm 0.3	6.9 \pm 3.4	-0.0	1.3	1.2	2.9 \pm 1.0
Jan. 28, 1998	2	14512	12	0.3 \pm 0.5	-2.6 \pm 4.6	0.4	1.5	0.6	1.7 \pm 1.4
April 08, 1998	2	15514	6	1.9 \pm 0.5	-8.8 \pm 5.9	0.5	2.0	0.8	0.9 \pm 1.8
May 13, 1998	2	16015	14	-0.2 \pm 0.3	4.6 \pm 3.9	-0.0	1.1	-0.1	0.3 \pm 1.2
July 22, 1998	2	17017	14	-0.4 \pm 0.3	0.6 \pm 3.5	0.0	0.2	-0.6	-0.1 \pm 1.1
Aug. 25, 1998	1	37191	10	-0.2 \pm 0.3	4.1 \pm 3.7	-0.1	-0.6	-1.0	0.1 \pm 1.1
Aug. 26, 1998	2	17518	16	-1.5 \pm 0.3	2.1 \pm 3.5	-0.2	-0.1	-1.7	-0.7 \pm 1.0
Nov. 04, 1998	2	18520	15	1.3 \pm 0.3	8.4 \pm 3.6	0.1	0.7	0.6	2.5 \pm 1.1
Dec. 09, 1998	2	19021	14	0.4 \pm 0.4	2.4 \pm 4.0	-0.1	1.8	0.4	0.7 \pm 1.2
Jan. 13, 1999	2	19522	11	0.4 \pm 0.4	6.1 \pm 4.5	0.1	0.8	-0.0	0.4 \pm 1.3

Dates and orbit, number of computed interferograms (N_{inter}), and modeling results with standard deviation errors are given: maximum delay (F_{cal}), relative volume of magma chamber (V), and tropospheric delay profile, expressed in half wavelength (equivalent to a fringe). Note that all values are relative to the first image (orbit 05785).

Table 2. Parameters Associated With the 238 Interferograms

No.	Image 1	Image 2	Duration, days	AA, m	Q	$\Delta F_{\text{obs}} \pm \mathbf{S}$ (Fringe)	ΔF_{cal}
1	00985	01987	70	-898	2	0.8 ± 0.4	0.8
2	00985	02989	140	-183	1	0.0 ± 0.9	0.5
3	00985	06997	420	30	1	-1.1 ± 1.3	-0.2
4	00985	12508	805	32	1	-1.6 ± 1.3	-0.3
5	00985	15514	1015	-219	1	3.4 ± 1.2	3.1
6	00985	21660	69	80	2	0.3 ± 0.3	0.1
7	00985	22662	139	89	1	0.3 ± 1.0	0.5
8	01486	03490	140	46	1	1.3 ± 1.4	0.7
9	01486	07498	420	-93	1	1.1 ± 1.0	-0.1
10	01486	09001	525	-54	1	0.9 ± 1.4	1.4
11	01486	11005	665	-32	1	4.4 ± 2.2	1.8
12	01486	13009	805	46	1	2.3 ± 1.2	0.8
13	01486	16015	1015	-40	1	1.2 ± 1.3	0.7
14	01486	17017	1085	86	1	-0.9 ± 1.3	0.4
15	01486	17518	1120	1300	1	-1.4 ± 0.8	-0.6
16	01486	18520	1190	397	1	1.4 ± 1.1	2.1
17	01486	19021	1225	-34	1	-0.3 ± 1.5	1.2
18	01987	02989	70	-91	2	-0.1 ± 0.6	-0.3
19	01987	06997	350	35	1	0.0 ± 1.5	-0.9
20	01987	12508	735	35	1	-0.9 ± 1.3	-1.0
21	01987	15514	945	-291	1	2.3 ± 1.0	2.4
22	01987	22662	69	-140	2	0.5 ± 1.2	-0.2
23	02488	23163	69	46	2	0.1 ± 1.2	0.2
24	02989	15514	875	294	1	2.7 ± 1.2	2.6
25	03490	07498	280	-31	1	-0.2 ± 1.5	-0.9
26	03490	07999	315	58	1	-0.1 ± 0.9	-0.1
27	03490	13009	665	-2807	1	-0.8 ± 0.8	0.1
28	03490	17017	945	-75	1	0.4 ± 1.6	-0.3
29	03490	17518	980	-50	1	-1.3 ± 1.5	-1.4
30	03490	18520	1050	-38	1	1.4 ± 1.6	1.3
31	03490	37191	979	55	1	-0.1 ± 1.5	-0.1
32	05785	01486	1074	-35	1	-0.4 ± 2.2	-0.8
33	05785	03490	1214	-156	1	0.0 ± 1.0	-0.1
34	05785	07999	1529	93	1	0.8 ± 1.1	-0.2
35	05785	09793	280	-207	2	2.9 ± 0.7	2.9
36	05785	10795	350	59	2	0.3 ± 0.8	1.2
37	05785	11296	385	43	2	-0.5 ± 1.1	-0.9
38	05785	13009	1879	-148	1	0.5 ± 1.3	0.0
39	05785	17017	2159	-51	1	0.4 ± 1.7	-0.4
40	05785	17518	2194	-39	1	-1.9 ± 1.9	-1.5
41	05785	18520	2264	-31	1	1.5 ± 2.2	1.3
42	05785	21159	1073	-45	1	-3.9 ± 1.2	-2.5
43	05785	22161	1143	92	1	1.4 ± 1.8	-1.0
44	05785	23163	1213	35	1	-0.4 ± 1.7	-0.8
45	05785	37191	2193	85	1	-1.4 ± 1.5	-0.2
46	06286	01486	1039	31	1	-0.3 ± 1.8	0.1
47	06286	06787	35	51	3	-0.1 ± 0.6	0.0
48	06286	06997	1424	-37	1	0.1 ± 1.7	-0.4
49	06286	07498	1459	46	1	0.7 ± 1.3	0.0
50	06286	09001	1564	70	1	1.1 ± 1.8	1.5
51	06286	10003	1634	-53	1	1.4 ± 1.5	2.1
52	06286	10294	280	36	2	3.4 ± 1.6	2.8
53	06286	11005	1704	612	1	1.0 ± 1.0	1.9
54	06286	11797	385	300	2	3.3 ± 0.3	2.9
55	06286	12298	420	-37	1	1.3 ± 1.7	1.8
56	06286	12508	1809	-37	1	-0.7 ± 1.7	-0.5
57	06286	14512	1949	-48	0	0.5 ± 2.0	1.2
58	06286	16015	2054	82	1	0.4 ± 1.1	0.8
59	06286	19021	2264	133	0	-1.6 ± 1.2	1.3

Table 2. (continued)

No.	Image 1	Image 2	Duration, days	AA, m	Q	$\Delta F_{\text{obs}} \pm \mathbf{S}$ (Fringe)	ΔF_{cal}
60	06286	19522	2299	-76	1	-0.2 ± 1.3	1.4
61	06787	01486	1004	75	1	0.1 ± 1.3	0.2
62	06787	07498	1424	400	1	-1.1 ± 1.3	0.0
63	06787	09001	1529	-192	0	2.0 ± 1.4	1.6
64	06787	10294	245	123	2	3.6 ± 0.7	2.8
65	06787	11005	1669	-56	1	1.1 ± 1.2	1.9
66	06787	11797	350	-62	2	2.6 ± 0.7	2.9
67	06787	16015	2019	-109	1	0.8 ± 1.3	0.8
68	06787	17017	2089	37	1	2.5 ± 1.7	0.6
69	06787	17518	2124	76	1	-0.1 ± 1.2	-0.5
70	06787	18520	2194	72	1	1.0 ± 1.7	2.2
71	06787	19021	2229	-72	1	1.7 ± 1.7	1.4
72	06787	21159	1003	52	1	-2.2 ± 1.9	-1.5
73	06997	10003	210	126	2	2.8 ± 0.4	2.5
74	06997	11005	280	35	1	2.4 ± 1.0	2.3
75	06997	12508	385	-10^4	2	0.4 ± 0.8	-0.1
76	06997	14512	525	166	1	0.4 ± 1.5	1.6
77	06997	19522	875	46	1	0.5 ± 1.5	1.8
78	07498	09001	105	-130	1	2.4 ± 1.3	1.5
79	07498	11005	245	-49	2	2.2 ± 0.6	1.9
80	07498	13009	385	31	1	1.4 ± 1.1	0.9
81	07498	16015	595	-78	1	1.0 ± 0.7	0.8
82	07498	17017	665	43	1	0.1 ± 0.7	0.5
83	07498	17518	700	92	2	-0.8 ± 0.6	-0.5
84	07498	18520	770	85	1	3.1 ± 0.8	2.2
85	07498	19021	805	-57	1	1.7 ± 1.1	1.3
86	07999	13009	350	-57	1	0.4 ± 0.9	0.1
87	07999	17017	630	-31	1	0.5 ± 1.9	-0.2
88	07999	37191	664	-990	1	0.2 ± 0.5	0.0
89	09001	10003	70	-30	2	-0.2 ± 1.7	0.6
90	09001	11005	140	-79	1	0.7 ± 1.5	0.4
91	09001	16015	490	-231	1	0.5 ± 1.5	-0.7
92	09001	17017	560	32	1	0.8 ± 2.3	-1.0
93	09001	17518	595	56	1	-3.0 ± 1.4	-2.0
94	09001	18520	665	53	1	0.6 ± 1.3	0.7
95	09001	19021	700	-110	1	1.0 ± 1.4	-0.2
96	09001	19522	735	-35	1	0.1 ± 2.0	-0.2
97	09793	01486	794	-42	1	-6.0 ± 1.7	-3.7
98	09793	03490	934	-634	1	-3.2 ± 1.1	-3.0
99	09793	07999	1249	64	1	-3.2 ± 1.3	-3.1
100	09793	10294	35	-35	2	-1.3 ± 0.9	-1.1
101	09793	10795	70	46	2	-1.4 ± 0.6	-1.7
102	09793	11296	105	36	2	-3.5 ± 0.9	-3.8
103	09793	13009	1599	-517	1	-3.5 ± 1.0	-2.9
104	09793	17017	1879	-67	1	-2.7 ± 1.7	-3.3
105	09793	17518	1914	-47	1	-3.6 ± 1.6	-4.4
106	09793	18520	1984	-40	1	-2.2 ± 1.6	-1.7
107	09793	21159	793	-57	1	-6.0 ± 1.6	-5.4
108	09793	22161	863	64	1	-3.9 ± 1.2	-3.9
109	09793	23163	933	30	1	-2.9 ± 1.6	-3.8
110	09793	37191	1913	55	1	-2.6 ± 1.4	-3.1
111	10003	11005	70	49	2	-0.1 ± 0.6	-0.2
112	10003	12508	175	-125	2	-3.2 ± 1.1	-2.6
113	10003	14512	315	-532	1	0.2 ± 1.4	-0.9
114	10003	16015	420	31	1	-0.8 ± 1.1	-1.3
115	10003	17518	525	20	1	-2.5 ± 2.2	-2.6
116	10003	19021	630	36	1	-1.2 ± 1.1	-0.8
117	10003	19522	665	85	1	-0.3 ± 0.8	-0.8
118	10294	01486	759	195	1	-2.1 ± 1.0	-2.7
119	10294	03490	899	37	1	-0.7 ± 1.5	-1.9

Table 2. (continued)

No.	Image 1	Image 2	Duration, days	AA, m	Q	$\Delta F_{\text{obs}} \pm \mathbf{S}$ (Fringe)	ΔF_{cal}
120	10294	07498	1179	-177	1	-2.9 ± 0.8	-2.8
121	10294	09001	1284	-75	1	-1.1 ± 1.5	-1.3
122	10294	11005	1424	-38	1	-0.6 ± 1.2	-0.9
123	10294	11797	105	-41	2	-0.2 ± 0.7	0.1
124	10294	13009	1564	37	1	-1.4 ± 1.8	-1.9
125	10294	16015	1774	-53	1	-1.5 ± 1.4	-2.0
126	10294	17017	1844	55	1	-1.9 ± 1.0	-2.3
127	10294	17518	1879	179	1	-4.3 ± 0.8	-3.3
128	10294	18520	1949	110	1	-0.6 ± 1.2	-0.6
129	10294	19021	1984	-43	1	-0.9 ± 1.7	-1.5
130	10294	21159	758	89	1	-3.5 ± 0.9	-4.4
131	10795	02488	794	30	1	-3.7 ± 2.3	-2.2
132	10795	03490	864	-43	1	-0.7 ± 1.8	-1.3
133	10795	07999	1179	-162	1	-2.2 ± 1.6	-1.3
134	10795	11296	35	157	3	-2.1 ± 0.2	-2.1
135	10795	13009	1529	-42	1	-1.9 ± 1.5	-1.2
136	10795	22161	793	-164	1	-1.6 ± 1.1	-2.1
137	10795	23163	863	89	1	-0.6 ± 1.3	-2.0
138	10795	37191	1843	-270	1	-1.3 ± 1.0	-1.4
139	11005	12508	105	-35	2	-2.3 ± 1.1	-2.4
140	11005	14512	245	-45	1	-1.0 ± 1.7	-0.7
141	11005	16015	350	102	2	-1.1 ± 0.5	-1.1
142	11005	19021	560	174	1	-0.7 ± 1.0	-0.6
143	11005	19522	595	-117	1	0.0 ± 1.0	-0.5
144	11296	02488	759	37	1	-0.7 ± 1.6	-0.1
145	11296	03490	829	-34	1	-1.1 ± 1.9	0.8
146	11296	07999	1144	-80	1	2.0 ± 1.1	0.7
147	11296	13009	1494	-33	1	1.5 ± 1.7	0.9
148	11296	22161	758	-80	1	0.4 ± 1.2	-0.1
149	11296	23163	828	204	1	-0.3 ± 0.8	0.0
150	11296	37191	1808	-77	1	-0.1 ± 1.2	0.7
151	11797	01486	654	34	1	-1.9 ± 1.5	-2.8
152	11797	06997	1039	-33	1	-2.0 ± 1.7	-3.3
153	11797	07498	1074	54	1	-3.3 ± 1.2	-2.9
154	11797	09001	1179	92	1	0.2 ± 1.7	-1.4
155	11797	10003	1249	-45	1	-1.3 ± 1.4	-0.8
156	11797	11005	1319	-589	1	-0.8 ± 1.2	-1.0
157	11797	12298	35	-33	2	-0.2 ± 1.1	-1.1
158	11797	12508	1424	-33	1	-2.1 ± 1.6	-3.4
159	11797	14512	1564	-42	0	-0.6 ± 2.1	-1.7
160	11797	16015	1669	114	1	-2.4 ± 1.4	-2.1
161	11797	18520	1844	31	1	-0.2 ± 2.1	-0.7
162	11797	19021	1879	250	1	-0.7 ± 1.7	-1.6
163	11797	19522	1914	-62	1	-0.7 ± 1.6	-1.5
164	12298	00985	584	-34	1	0.5 ± 1.8	-2.0
165	12298	01987	654	-35	1	-2.0 ± 1.5	-1.2
166	12298	06997	1004	2406	1	-1.3 ± 1.3	-2.2
167	12298	10003	1214	120	1	0.7 ± 0.8	0.4
168	12298	11005	1284	35	1	-0.9 ± 1.9	0.1
169	12298	12508	1389	3104	1	-2.9 ± 1.0	-2.3
170	12298	14512	1529	155	0	0.1 ± 1.7	-0.5
171	12298	19522	1879	58	1	-0.5 ± 1.7	-0.4
172	12298	20658	583	-75	1	-0.8 ± 1.2	0.1
173	12298	21660	653	-57	1	-0.5 ± 1.4	-1.9
174	12298	22662	723	-47	1	-1.7 ± 1.2	-1.5
175	12508	14512	140	163	1	1.9 ± 1.5	1.7
176	12508	19522	490	42	1	1.7 ± 0.9	1.9
177	13009	17017	280	-72	1	-0.2 ± 0.6	-0.4
178	13009	17518	315	-51	2	-1.0 ± 0.8	-1.4
179	13009	18520	385	-40	1	1.6 ± 0.8	1.3

Table 2. (continued)

No.	Image 1	Image 2	Duration, days	AA, m	Q	$\Delta F_{\text{obs}} \pm \mathbf{S}$ (Fringe)	ΔF_{cal}
180	13009	37191	314	55	1	0.1 ± 0.8	-0.2
181	14512	19021	315	33	1	1.0 ± 1.8	0.1
182	14512	19522	350	108	1	1.0 ± 1.7	0.1
183	16015	17518	105	45	2	-0.7 ± 1.0	-1.3
184	16015	18520	175	35	2	1.7 ± 0.8	1.4
185	16015	19021	210	-251	1	1.7 ± 1.0	0.5
186	16015	19522	245	-54	1	0.0 ± 1.2	0.6
187	17017	17518	35	-133	3	-0.8 ± 0.4	-1.0
188	17017	18520	105	-109	2	1.8 ± 0.4	1.7
189	17518	18520	70	-359	2	2.7 ± 0.1	2.7
190	17518	19021	105	-37	1	2.2 ± 1.4	1.8
191	18520	19021	35	-36	2	-1.3 ± 1.4	-0.9
192	19021	19522	35	-70	2	0.1 ± 1.3	0.0
193	20658	00985	1	-63	4	-2.4 ± 0.5	-2.1
194	20658	01987	71	-66	2	-1.5 ± 0.6	-1.3
195	20658	02989	141	-38	1	-0.7 ± 1.1	-1.6
196	20658	06997	421	72	1	-1.5 ± 1.0	-2.3
197	20658	10003	631	46	1	1.2 ± 1.2	0.3
198	20658	12508	806	73	1	-2.0 ± 0.9	-2.3
199	20658	14512	946	50	0	0.8 ± 1.8	-0.6
200	20658	15514	1016	-49	1	1.9 ± 1.2	1.0
201	20658	21660	70	-246	2	-2.0 ± 0.2	-1.9
202	20658	22662	140	-127	1	-1.9 ± 0.8	-1.5
203	21159	01486	1	-164	4	1.7 ± 0.4	1.7
204	21159	03490	141	63	1	1.1 ± 1.2	2.5
205	21159	07498	421	-59	1	2.0 ± 0.5	1.6
206	21159	07999	456	30	1	1.5 ± 1.4	2.4
207	21159	09001	526	-41	1	3.1 ± 2.2	3.1
208	21159	13009	806	64	1	3.2 ± 0.8	2.5
209	21159	16015	1016	-31	1	3.1 ± 1.5	2.4
210	21159	17017	1086	210	1	2.8 ± 1.2	2.1
211	21159	17518	1121	-200	1	1.0 ± 1.1	1.1
212	21159	18520	1191	-228	1	3.1 ± 0.8	3.8
213	21159	22161	70	30	2	0.4 ± 1.3	1.6
214	21660	01987	1	-91	4	0.7 ± 0.2	0.6
215	21660	02989	71	-45	2	-0.2 ± 1.1	0.4
216	21660	06997	351	56	1	-0.6 ± 1.0	-0.3
217	21660	10003	561	39	1	2.3 ± 1.4	2.2
218	21660	12508	736	56	1	-0.3 ± 1.1	-0.4
219	21660	14512	876	42	1	1.1 ± 1.7	1.3
220	21660	15514	946	-59	1	2.4 ± 1.2	3.0
221	21660	22662	70	-262	2	0.2 ± 0.6	0.4
222	22161	02488	1	27	4	0.9 ± 1.4	-0.1
223	22161	03490	71	-58	2	0.9 ± 0.8	0.9
224	22161	07999	386	-10 ⁴	1	0.9 ± 0.7	0.8
225	22161	13009	736	-57	1	1.7 ± 1.0	0.9
226	22161	17017	1016	-31	1	0.8 ± 1.5	0.5
227	22161	23163	70	58	2	-0.2 ± 1.3	0.1
228	22161	37191	1050	-921	1	-0.3 ± 1.2	0.7
229	22662	02989	1	-55	4	0.1 ± 0.9	0.0
230	22662	06997	281	46	1	-1.4 ± 1.4	-0.7
231	22662	10003	491	34	1	0.8 ± 1.3	1.8
232	22662	12508	666	46	1	-0.7 ± 0.9	-0.8
233	22662	14512	806	36	1	0.8 ± 2.0	0.9
234	22662	15514	876	-63	1	2.1 ± 1.2	2.6
235	23163	03490	1	-31	4	0.5 ± 1.4	0.8
236	23163	07999	316	-57	1	1.1 ± 1.1	0.7
237	23163	37191	980	-49	1	1.4 ± 1.4	0.6
238	37191	17518	1	-29	4	-0.7 ± 1.0	-1.2

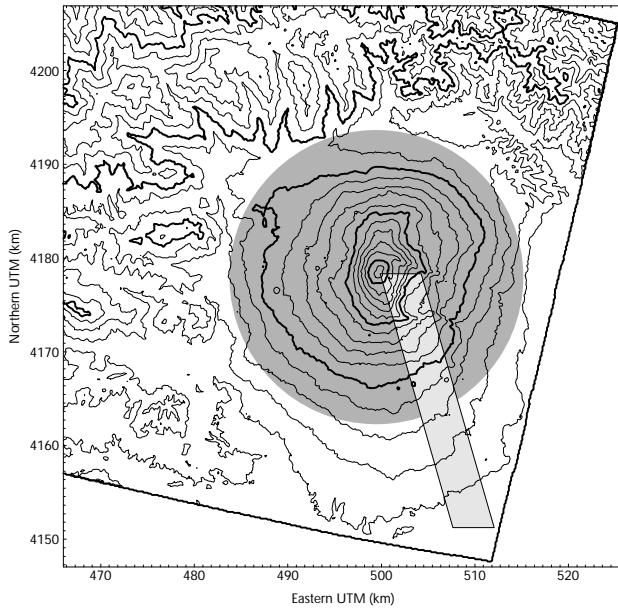


Figure 1. Contour map of Mount Etna in universal transverse mercator (UTM) projection (WGS 84). Wide lines are every 1000 m. Shaded circle indicates the “Etna” area limit with the “around” area. Light grey parallelogram represents the selected zone (100×1200 pixels) from Catania to summit for fringe automatic counting.

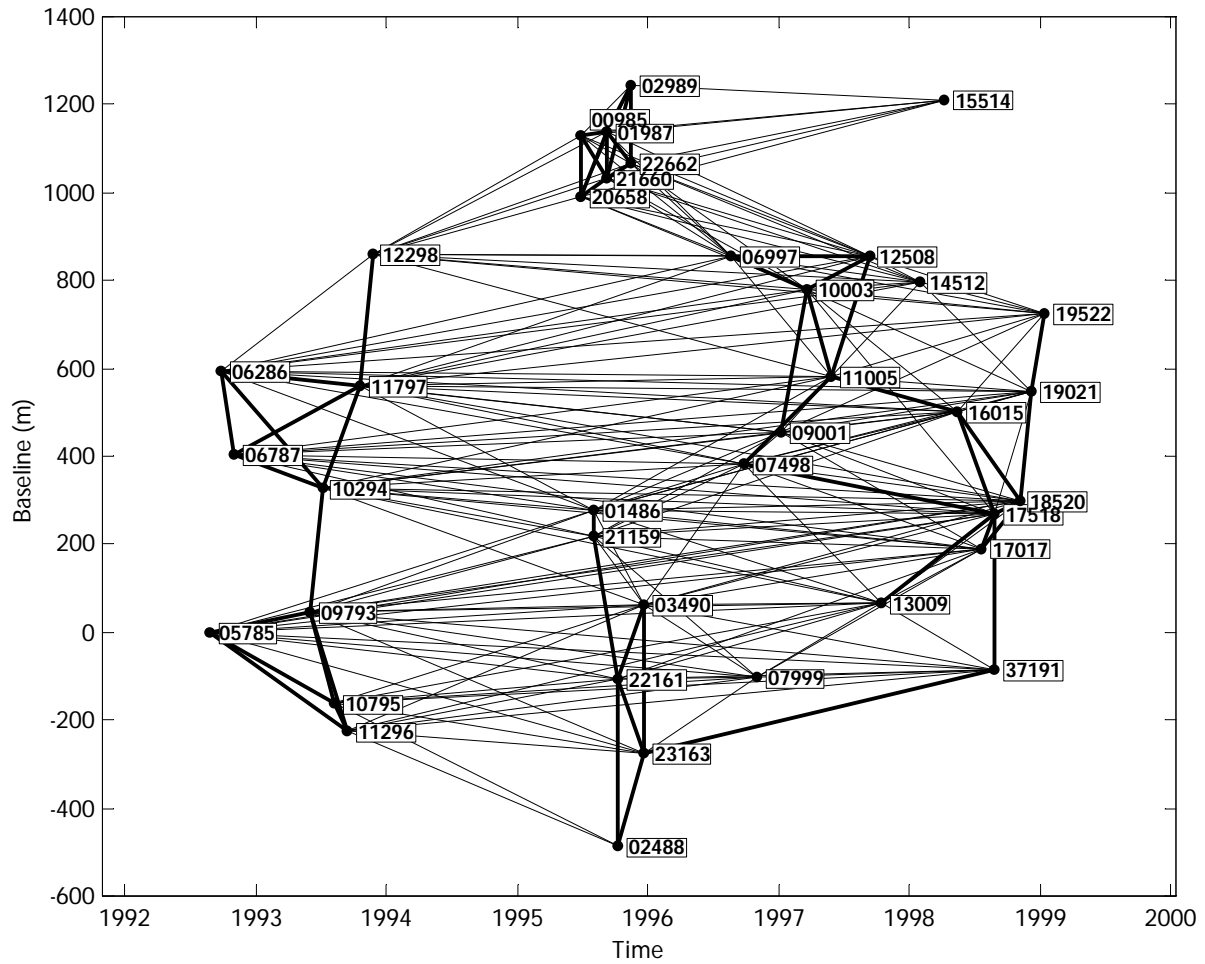


Figure 2. SAR images set and interferograms used, represented as baseline values versus date time take. Black dots and numbers are the 38 images with their associated orbits. Reference baseline is 05785 orbit. Solid lines are the 238 computed interferograms (dark lines stand for a good quality of coherence, $Q \geq 2$).

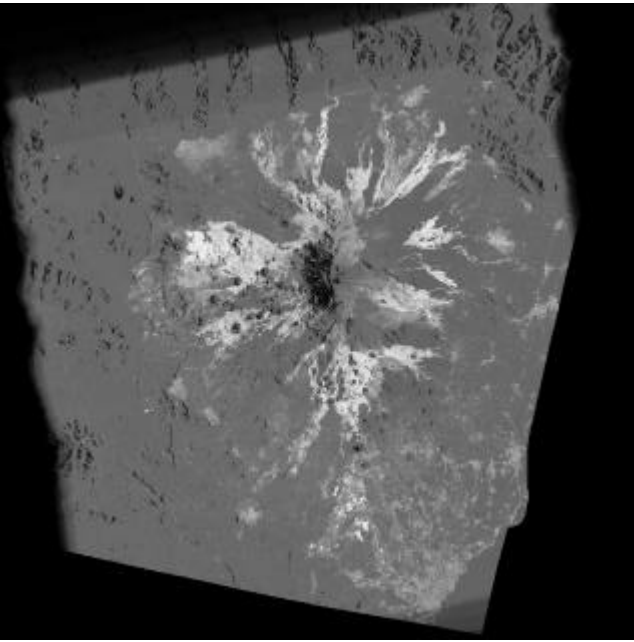


Figure 3. Collective coherency map computed from the 238 interferograms over the 1992 to 1999 period. Greyscale stands for average coherency (from black, indicating no coherency, to white, indicating maximum of coherency). The coherency remains high in average especially for the main lava flows and towns (permanent scatters). This map is used to calculate the collective mask (CM) that is applied to data for filtering.

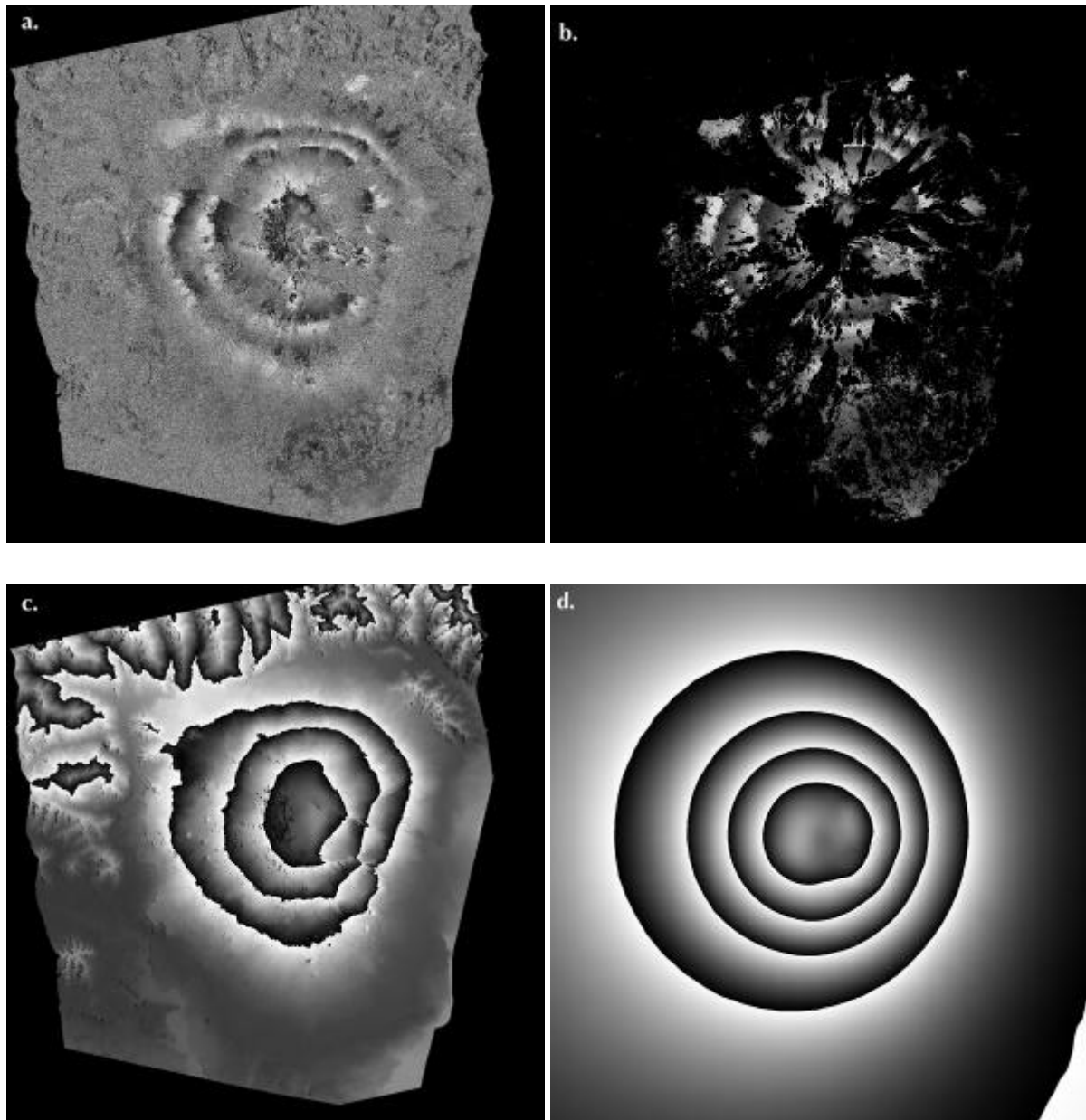


Figure 4. Example of interferogram data and processing: interferogram 54, September 27, 1992 (06286), to October 17, 1993 (11797). (a) Original data. (b) Data kept after filtering with the CM. (c) Tropospheric and deformation modeling proposed in this paper. (d) Deformation 3-D elastic modeling (deflation source) previously proposed [Cayol and Cornet, 1998].

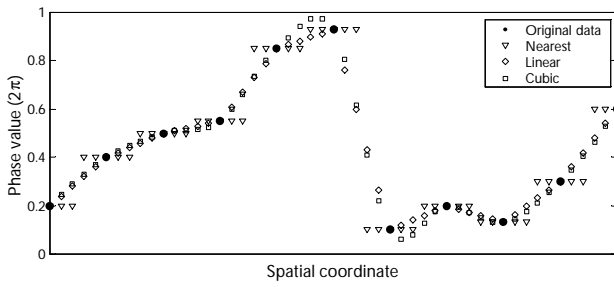


Figure 5. A 1-D example of different interpolation methods on wrapped data: only the nearest-neighbor method keeps the phase jumps intact.

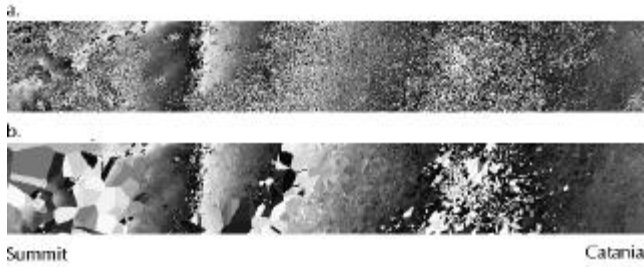


Figure 6. Example of interpolation by the nearest neighbor method on the selected area (1200×100 pixels) from Catania to summit (interferogram 54). (a) Original phase values. (b) Interpolated data after the applying of collective mask. Note the unsmoothed phase wrapping (transitions black to white) that are kept intact and will favor phase unwrapping.

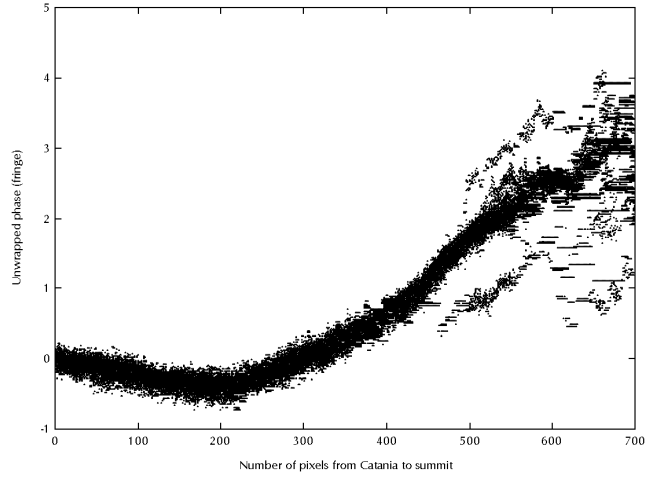


Figure 7. Example of unwrapped phase along the 100 parallel profiles from Catania to summit (interferogram 54). Maximum number of fringes and the associated uncertainty are determined by the average and standard deviation of all the profiles end phases.

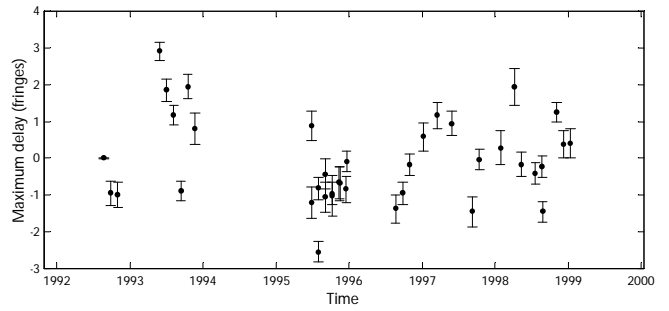


Figure 8. Maximum number of fringes (from Catania to summit) compensated for each image (see also Table 1). Note the annual negative peak (except for 1994, for which no data are available) that may be associated to meteorological effect.

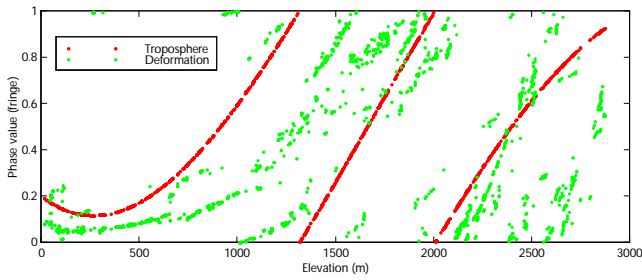


Figure 9. Theoretical phase-elevation relation for troposphere and deformation simple models (three fringes observed from sealevel to summit), computed for the 1686 pixels selected in this paper (see Figure 10). A horizontally layered troposphere produces values of phase delay as a function of elevation (solid dots). For a deflation point source in half-space elastic medium [Mogi, 1958], phases cannot be directly related to elevation (shaded dots) because of the asymmetry of Etna edifice and projection of the displacements on satellite line of sight. This difference in pattern allows us to distinguish the effects due to a source of deformations from those due to a layered troposphere.

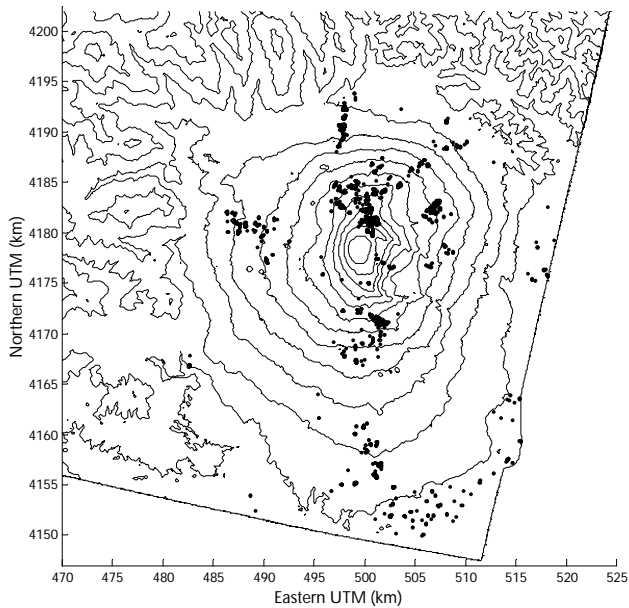


Figure 10. Equally spaced altitude mask (ESAM), location of the 1686 selected pixels for the modeling of deformation and troposphere effects (20 most coherent pixels for each vertical 50-m layer).

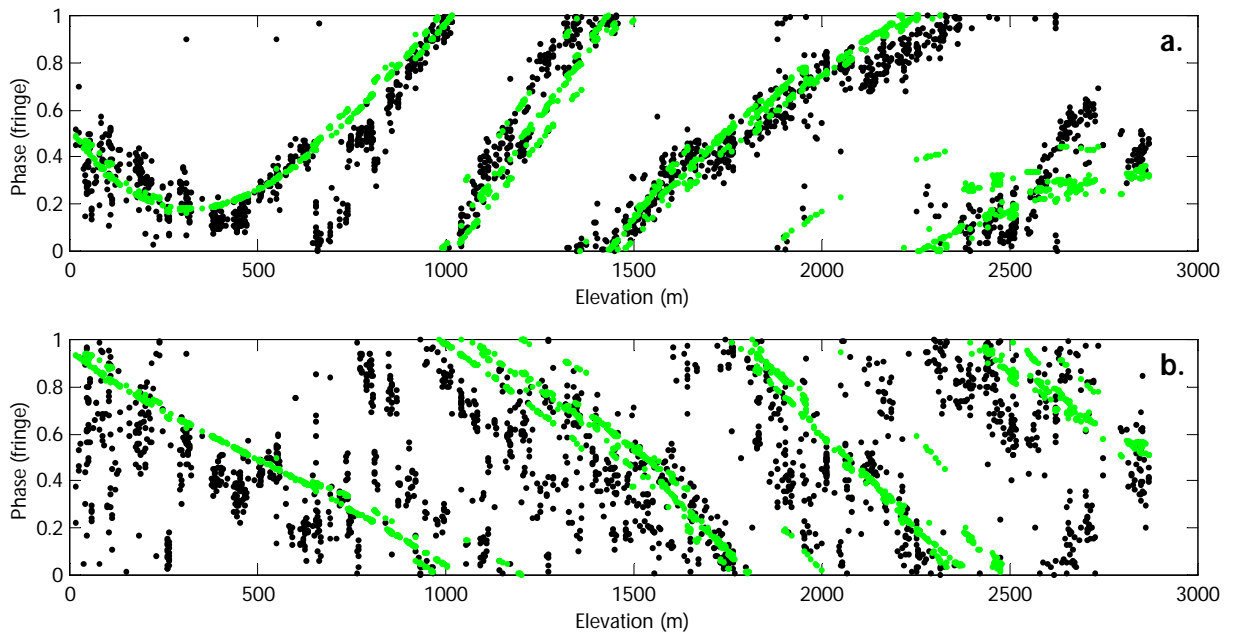


Figure 11. Examples of phase-elevation data and modeling. (a) Interferogram 54, $\Delta V = -3.9 \times 10^6 \text{ m}^3$, $\Delta T_{3000\text{m}} = +3.0$ fringes. Note the high correlation between phase and elevation. (b) Interferogram 108, $\Delta V = -3.8 \times 10^6 \text{ m}^3$, $\Delta T_{3000\text{m}} = -4.0$ fringes. Solid dots are original data selected by the equally spaced altitude mask, and shaded dots are the tropospheric and deformation modeled differential delays.

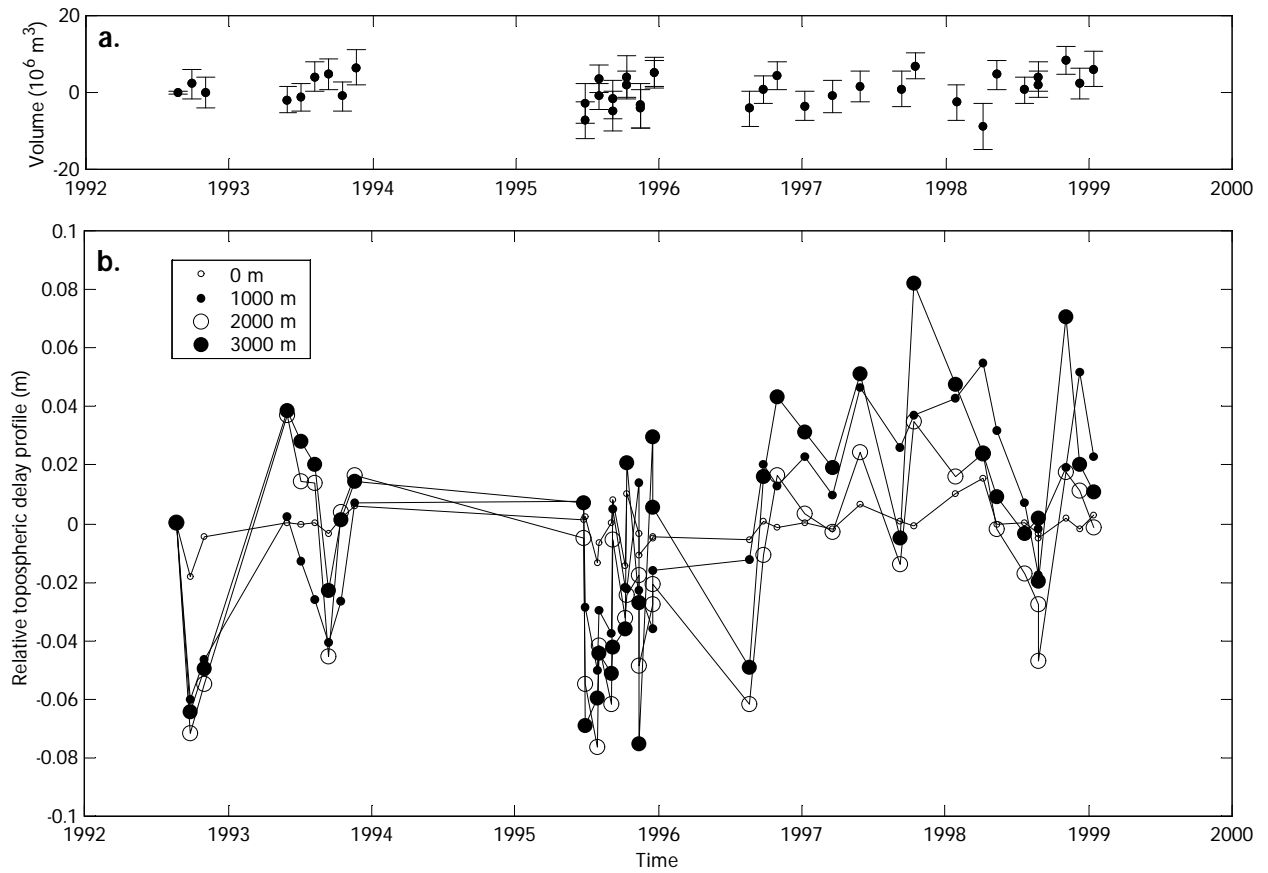


Figure 12. Results of final inversion: model for the source of deformations and tropospheric profiles for each SAR image. (a) Volume variations in 6-km-deep source below the summit and a posteriori errors (in millions of cubic meters). (b) Tropospheric delays (in meters) for each altitude layer (0 to 3000 m), relative to unknown tropospheric delay profile of the first image (orbit 05785).

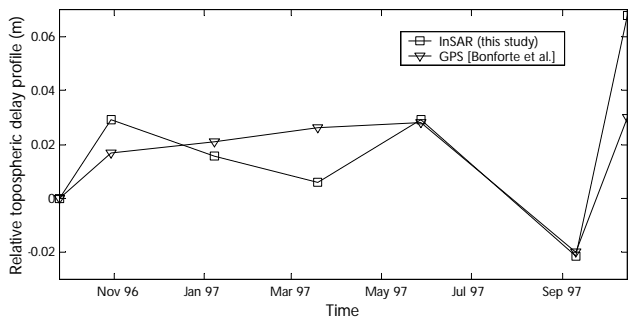


Figure 13. Comparison of tropospheric delay's at 3000 m modeled in this paper, and estimated from GPS measurements on Etna (A. Bonforte et al., submitted paper, 1999).

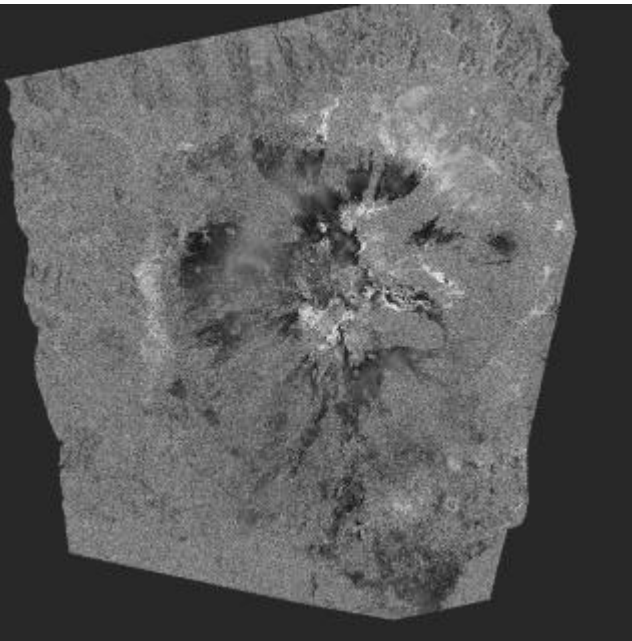


Figure 14. Example of residual obtained after tropospheric and deformation model removal (interferogram 54). The residual phase must be attributed to inhomogeneous tropospheric effects or local deformation.